

# Effects of coupling constants on chaos of charged particles in the Einstein-Æther theory

Caiyu Liu<sup>1,2</sup>, Xin Wu<sup>1,2†</sup>

<sup>1</sup>*School of Mathematics, Physics and Statistics, Shanghai University of Engineering Science, Shanghai 201620, China*

<sup>2</sup>*Center of Application and Research of Computational Physics, Shanghai University of Engineering Science, Shanghai 201620, China*

† Corresponding Author's Email: wuxin\_1134@sina.com

## ABSTRACT

There are two free coupling parameters  $c_{13}$  and  $c_{14}$  in the Einstein-Æther metric describing a non-rotating black hole. This metric is the Reissner-Nordström black hole solution when  $0 \leq 2c_{13} < c_{14} < 2$ , but it is not for  $0 \leq c_{14} < 2c_{13} < 2$ . When the black hole is immersed in an external asymptotically uniform magnetic field, the Hamiltonian system describing the motion of charged particles around the black hole is not integrable. However, the Hamiltonian allows for the construction of explicit symplectic integrators. The proposed fourth-order explicit symplectic scheme is used to investigate the dynamics of charged particles because it exhibits excellent long-term performance in conserving the Hamiltonian. No universal rule can be given to the dependence of regular and chaotic dynamics on varying one or two parameters  $c_{13}$  and  $c_{14}$  in the two cases of  $0 \leq 2c_{13} < c_{14} < 2$  and  $0 \leq c_{14} < 2c_{13} < 2$ . The distributions of order and chaos in the binary parameter space  $(c_{13}, c_{14})$  rely on different combinations of the other parameters and the initial conditions.

*Keywords:* Modified theory of gravity; Black holes; Magnetic field; Chaos; Symplectic integrator

## 1. Introduction

Detections of gravitational waves [1] and event-horizon-scale images of M87\* [2] have strongly supported the prediction of Einstein's general theory of relativity on the existence of black holes. Although the standard general relativity has attained the great success, its extension and development are still necessary because of its limits. One example is that the dark universe beyond the Einstein's theory may provide a good explanation for the apparent accelerating expansion of the

Universe. Another example is the difficulty of building a complete theory unifying interactions and particles in the general relativity and quantum mechanics. Such theories of gravity are called as extended, alternative or modified gravitational theories.

There are numerous modified gravitational theories in the literature. Some of them are scalar-tensor theories of gravity [3,4], scalar-tensor-vector theories [5,6], Hořava-Lifschitz gravity [7], Kaluza-Klein theories of gravity [8,9],  $F(R)$  gravity [10], quantum field theory in curved spacetime [7,11], and Einstein-Æther theories [12-14]. As far as the Einstein-Æther theories are concerned, they are obtained by coupling the Æther field with other fields, such as an electromagnetic field. They violate the Lorentz invariance that is one of the fundamental principles of Einstein's general relativity. The so-called Æther means the presence of Lorentz-violating vector fields. This particular property can dramatically affect cosmology, and can even affect the growth rate of structure in the Universe. See [15-17] for more information on these modified gravitational theories.

From the astrophysical perspective, it is interesting to study the motion of test particles around a black hole in the standard general relativity or a certain modified theory of gravity. The radiation emission by the particles with high energies in the accretion disk leads to the electromagnetic spectrum of astrophysical black hole. The spectrum is useful to understand the effects of Doppler and gravitational red-shift. Circular orbits and the innermost stable circular orbits (ISCOs) of the particles near the black hole can give some important astrophysical information on the nearby activity of the black hole. Thus, their studies have appeared in a large number of publications (see, e.g., [18-28]). The study of photon circular orbits also has a crucial application in astrophysics because the existence of photon circular orbits is closely related to the computation of black hole shadows [29-31]. When an external asymptotically uniform magnetic field is included in the vicinity of the black hole, the dynamics of electrically charged particles is nonintegrable in general and is even chaotic. In fact, there are lots of works about the presence of chaotic motions of charged particles around black holes (see, e.g., [32-39]). The chaotic charged particle dynamics is helpful for charged particle acceleration along the magnetic field lines [40]. Chaotic photon motions in non-integrable black hole spacetimes also give self-similar fractal structures to the black hole shadows [41,42].

Rayimbaev et al. [14] studied the effects of Einstein-Æther gravity on the dynamics of magnetized particles around a black hole surrounded by an external asymptotically uniform magnetic field in the equatorial plane. They mainly discussed the impacts of varying the free coupling parameters  $c_{13}$  and  $c_{14}$  of the Einstein-Æther theory on the radii of the ISCOs, the location of circular orbits, the amount of center-of-mass energy and the strength of the magnetic field. Unlike these authors, we consider in the present work how the two coupling parameters affect the dynamics of electrically charged particles in the 3-dimensional space rather than the equatorial plane. In addition, we design explicit symplectic integrators for the Hamiltonian system describing the motion

of charged particles near the Einstein-Æther black hole by following the recent works [43-47]. Such symplectic methods that maintain symplectic nature of Hamiltonian dynamics are the most appropriate solvers for studying the long-term evolution of Hamiltonian systems [48]. One of the proposed explicit symplectic integrators combined with chaos indications such as fast Lyapunov indicators (FLIS) [49] is used to explore the dependence of regular and chaotic dynamics on varying one or two parameters  $c_{13}$  and  $c_{14}$ .

The paper is organized as follows. In Section 2, we introduce the Einstein-Æther black hole metric and its corresponding Hamiltonian system. In Section 3, we establish explicit symplectic integrators and investigate the regular and chaotic dynamics of charged particles. Finally, results are summarized in Section 4.

## 2. Einstein-Æther black hole metric

Based on the action of Einstein-Æther theory, a metric describing a non-rotating black hole [14] is written in the Schwarzschild coordinates  $(t, r, \theta, \varphi)$  as

$$ds^2 = g_{\alpha\beta} dx^\alpha dx^\beta = -f dt^2 + f^{-1} dr^2 + r^2(d\theta^2 + \sin^2 \theta d\varphi^2), \quad (1)$$

$$f(r) = 1 - \frac{2M}{r} \left( 1 + \frac{2c_{13} - c_{14} M}{4(1 - c_{13}) r} \right). \quad (2)$$

Here,  $t$  is a coordinate time, and  $M$  is the mass of the black hole.  $c_{13} = c_1 + c_3$  and  $c_{14} = c_1 + c_4$  are two coupling constants of the Einstein-Æther theory. Of course,  $c_1, c_3, c_4$  and the following parameter  $c_2$  are still coupling constants. In fact, they are some of the coefficients in the tensor

$$M_{\mu\nu}^{\alpha\beta} = c_1 g_{\mu\nu} g^{\alpha\beta} + c_2 \delta_\mu^\alpha \delta_\nu^\beta + c_3 \delta_\nu^\alpha \delta_\mu^\beta - c_4 u^\alpha u^\beta g_{\mu\nu}, \quad (3)$$

which determines the Lagrangian of Æther field

$$\mathcal{L}_x = -M_{\mu\nu}^{\alpha\beta} (D_\alpha u^\mu)(D_\beta u^\nu) + \Lambda(g_{\mu\nu} u^\mu u^\nu + 1) \quad (4)$$

in the action

$$S_x = \frac{1}{16\pi G_x} \int d^4x \sqrt{-g} (\mathcal{R} + \mathcal{L}_x). \quad (5)$$

$G_x = G_N/(1 - c_{14}/2)$  is the Æther gravitational constant, where  $G_N$  stands for the Newtonian gravitational constant.  $D_\alpha$  denotes the covariant derivative with respect to  $x^\alpha$ ,  $\Lambda$  is the Lagrangian multiplier, and  $u^\alpha$  is the Æther four-velocity.  $g = |g_{\mu\nu}|$ , and  $\mathcal{R}$  is the curvature. When the coupling constants  $c_{13}$  and  $c_{14}$  are given different values, Equation (1) represents different spacetimes. Here, three cases are listed. Case (i): if  $c_{14} = 2c_{13} \neq 2$ , Eq. (1) is the Schwarzschild metric. Case (ii):

when  $0 \leq c_{13} < 1$  and  $2c_{13} < c_{14} < 2$ , Eq. (1) represents the Reissner-Nordström (RN) black hole with the electric charge

$$Q = M\sqrt{(c_{14} - 2c_{13})/[2(1 - c_{13})]} \quad (6)$$

and two horizons

$$R_h^\pm = M \left( 1 \pm \sqrt{(2 - c_{14})/[2(1 - c_{13})]} \right). \quad (7)$$

Case (iii): if  $0 \leq c_{13} < 1$  and  $0 \leq c_{14} < 2c_{13} < 2$ , Equation (1) shows that the black hole with one horizon  $R^+$  has no electric charge and is not the RN black hole. In the three cases, the coupling constants  $c_{13}$  and  $c_{14}$  satisfy the constraints  $0 \leq c_{13} < 1$  and  $0 \leq c_{14} < 2$  from theoretical and observational bounds [14], which correspond to the presence of one or two horizons. The speed of light  $C$  and Newton's constant of gravity  $G_N$  are given geometrized units,  $C = G_N = 1$ .

Consider that an external asymptotically uniform magnetic field exists in the vicinity of black hole. This magnetic field is static, axially symmetric and homogeneous at the spatial infinity, and has its strength  $B > 0$  at the spatial infinity. It is so weak that it does not affect the spacetime geometry. Based on the Wald's method, only one non-vanishing component of the electromagnetic four potential was given in Ref. [14] by

$$A_\phi = \frac{1}{2}Br^2 \sin^2 \theta. \quad (8)$$

Although such a weak magnetic field exerts a negligible influence on the spacetime geometry, it plays an important role in the motion of a charged test particle with mass  $m$  and charge  $q$ . The motion is described by the following Hamiltonian

$$H = \frac{1}{2m}g^{\mu\nu}(p_\mu - qA_\mu)(p_\nu - qA_\nu), \quad (9)$$

where the momentum  $p_\mu$  satisfies the condition

$$\dot{x}^\mu = \frac{\partial H}{\partial p_\mu} = \frac{1}{m}g^{\mu\nu}(p_\nu - qA_\nu), \quad (10)$$

or an equivalent form

$$p_\mu = mg_{\mu\nu}\dot{x}^\nu + qA_\mu. \quad (11)$$

The four-velocity  $\dot{x}^\mu = (\dot{t}, \dot{r}, \dot{\theta}, \dot{\phi})$  is a derivative of coordinate  $x^\mu$  with respect to the proper time  $\tau$ .

To simplify the expressions, we adopt dimensionless operations through scale transformations as follows:  $t \rightarrow tM$ ,  $\tau \rightarrow \tau M$ ,  $r \rightarrow rM$ ,  $B \rightarrow B/M$ ,  $E \rightarrow mE$ ,  $p_t \rightarrow mp_t$ ,  $p_r \rightarrow mp_r$ ,  $L \rightarrow MmL$ ,



$p_\theta \rightarrow Mmp_\theta$ ,  $q \rightarrow mq$ , and  $H \rightarrow mH$ . In this case,  $m$  and  $M$  as two mass factors are eliminated in the above expressions.

Because the Hamiltonian (9) does not explicitly depend on the coordinates  $t$  and  $\varphi$ ,  $p_t$  and  $p_\varphi$  are constants of motion, which correspond to the energy  $E$  and angular momentum  $L$  of the particle:

$$p_t = -ft = -E, \quad (12)$$

$$p_\varphi = r^2 \sin^2 \theta \dot{\varphi} + qA_\varphi = L. \quad (13)$$

The Hamiltonian (9) is rewritten as

$$H = T + V, \quad (14)$$

$$T = \frac{p_r^2}{2} - \frac{p_r^2}{r} + \frac{p_\theta^2}{2r^2} - \frac{p_r^2(2c_{13} - c_{14})}{4r^2(1 - c_{13})}, \quad (15)$$

$$V = \frac{L^2}{2r^2 \sin^2 \theta} + \frac{b^2 r^2}{8} + \frac{bL}{2 \sin \theta} + \frac{E^2 r^2 (1 + c_{13})}{2c_{13} - c_{14} + 4(1 - c_{13})r - 2(1 - c_{13})r^2}, \quad (16)$$

where  $b = Bq$ . Noticing that the four-velocity  $\dot{x}^\mu$  always satisfies the relation  $g_{\mu\nu}\dot{x}^\mu\dot{x}^\nu = -1$  for a timelike geodesic, we have a third motion constant

$$H = -\frac{1}{2}. \quad (17)$$

### 3. Numerical simulations

At first, we introduce how to design explicit symplectic integrators for the Hamiltonian (14). Then, an appropriate one of the integrators is used to study the regular and chaotic dynamics of charged particles near the black hole.

#### 3.1. Explicit symplectic integrations

As the authors of [44] claimed, the Hamiltonian (14) can be split into five parts

$$H = H_1 + H_2 + H_3 + H_4 + H_5 \quad (18)$$

where these sub-Hamiltonian systems are

$$H_1 = V, \quad (19)$$

$$H_2 = \frac{p_r^2}{2}, \quad (20)$$

$$H_3 = -\frac{p_r^2}{r}, \quad (21)$$

$$H_4 = \frac{p_\theta^2}{2r^2}, \quad (22)$$

$$H_5 = \frac{p_r^2(c_{14} - 2c_{13})}{4r^2(1 - c_{13})}. \quad (23)$$

The five splitting parts are solved analytically and their analytical solutions are explicit functions of the proper  $\tau$ . Operators for analytically solving these sub-Hamiltonians are  $\mathcal{H}_1, \mathcal{H}_2, \mathcal{H}_3, \mathcal{H}_4$  and  $\mathcal{H}_5$  in turn. The five-splitting-part method is based on the exclusion of Case (i) with  $c_{14} = 2c_{13}$ .

Setting  $h$  as a time step, we have a second-order explicit symplectic algorithm for the Hamiltonian (14)

$$\begin{aligned} S_2(h) = & \mathcal{H}_5\left(\frac{h}{2}\right) \times \mathcal{H}_4\left(\frac{h}{2}\right) \times \mathcal{H}_3\left(\frac{h}{2}\right) \times \mathcal{H}_2\left(\frac{h}{2}\right) \times \mathcal{H}_1(h) \\ & \times \mathcal{H}_2\left(\frac{h}{2}\right) \times \mathcal{H}_3\left(\frac{h}{2}\right) \times \mathcal{H}_4\left(\frac{h}{2}\right) \times \mathcal{H}_5\left(\frac{h}{2}\right). \end{aligned} \quad (24)$$

In such a construction, the sub-Hamiltonian  $H_5$  is integrated by advancing the time  $h/2$ . When the obtained solutions are taken as the initial conditions, we solve the sub-Hamiltonian  $H_4$  by advancing the time  $h/2$ . The operation is also applied to the sub-Hamiltonians  $H_3$  and  $H_2$ . Taking the numerical solutions at the time as the initial conditions, we work out the sub-Hamiltonian  $H_1$  by advancing the time  $h$ . Then, we continue to solve the sub-Hamiltonian  $H_2, H_3, H_4$  and  $H_5$  in sequence by advancing the time  $h/2$ . As a result, the numerical solutions are outputted in one integration step. According to the idea of Yoshida [50], the second-order explicit symplectic integrator can be risen to a fourth-order algorithm

$$S_4 = S_2(\gamma h) \times S_2(\delta h) \times S_2(\gamma h), \quad (25)$$

where  $\gamma = 1/(2 - \sqrt[3]{2})$  and  $\delta = 1 - 2\gamma$ . This construction is explained as follows. We use the algorithm  $S_2$  to act on the Hamiltonian (18) by advancing the time  $\gamma h$ . Taking the numerical solutions as the initial conditions, we continue to solve the Hamiltonian (18) by using the algorithm  $S_2$  in a span of time  $\delta h$ . Finally, we repeat to use the algorithm  $S_2$  to integrate the Hamiltonian (18) by advancing the time  $\gamma h$ . In this way,  $\gamma h + \delta h + \gamma h = h$ ; that is, one step computation finishes.

In our numerical tests, the fixed proper time step  $h = 1$  is used. The parameters are given by  $E = 0.995$ ,  $L = 4.7$  and  $b = 9.1 \times 10^{-4}$ . The coupling constants are taken as  $c_{13} = 0.01$  and

$c_{14} = 0.03$ . The initial conditions are  $p_r = 0$  and  $\theta = \pi/2$ . Given the initial separation  $r$ , the initial value of  $p_\theta (> 0)$  is determined in terms of Equations (14)-(17). The initial separations are  $r = 15$  for Orbit 1 and  $r = 35$  for Orbit 2. When the two orbits are integrated by the second-order method  $S_2$  and the fourth-order method  $S_4$ , Hamiltonian errors  $\Delta H = H + 1/2$  are plotted in Figure 1 (a) and (b). These errors show no secular drift with time. This property is an advantage of symplectic integrators. Of course, the errors are sensitive dependence on the step choice. They decrease with a decrease of the time step. However, extremely small steps are not permitted due to the increase of computational cost and the rapid accumulation of roundoff errors. Relatively large steps are not, either, because they lead to large errors and make the algorithms unstable. The time step  $h = 1$  is an appropriate choice in the present problem. Clearly,  $S_4$  is superior to  $S_2$  in accuracy. Thus, it will be employed in the later computations.

In fact, Orbit 1 is regular and Orbit 2 is chaotic. The regularity or chaoticity is seen from the Poincaré map in the two-dimensional  $r - p_r$  plane in Figure 1 (c). All points in the two-dimensional plane are intersections of the particles' trajectories with the surface of section  $\theta = \pi/2$  with  $p_\theta > 0$  in phase space. The regular dynamics of Orbit 1 is shown because the points in the surface of section form a closed curve, which corresponds to a cross section of a torus in the phase space. The chaotic dynamics of Orbit 2 is known by the points that are distributed randomly in the Poincaré map. The Poincaré map method is a good description of the regular and chaotical dynamical structure of trajectories in a conservative four-dimensional phase space. The algorithms  $S_2$  and  $S_4$  exhibit good long-term performance in the conservation of the Hamiltonian (14) or (18), irrespective of whether or not the integrated orbit is chaotic.

### 3.2. Orbital dynamics

In addition to the Poincaré map method, Lyapunov exponents and fast Lyapunov indicators (FLIs) are common methods to detect chaos from order. The maximal Lyapunov exponent corresponding to the most unstable direction in the phase space directly measures how the given orbit is sensitive dependence on the initial conditions. It is defined in [51] as an invariant indicator of chaos under spacetime coordinate transformations within the relativistic framework

$$\lambda = \lim_{\tau \rightarrow \infty} \ln \frac{1}{\tau} \frac{d(\tau)}{d(0)}, \quad (26)$$

where  $d(\tau)$  and  $d(0)$  are the proper distances of two nearby orbits at the proper time  $\tau$  and the starting time, respectively.  $\lambda$  tends to zero for a bounded, regular orbit, while it attains a positive value for a bounded, chaotic orbit. The distinct evolution tendency of  $\lambda$  can distinguish between chaotic and regular orbits. Based on this point, the regular dynamics of Orbit 1 and the chaotic dynamics of Orbit 2 are confirmed by the maximal Lyapunov exponents in Figure 2 (a). The FLI

is a quicker method to detect chaos and quasiperiodicity than the largest Lyapunov exponent. Its invariant definition [52] is

$$FLI = \log_{10} \frac{d(\tau)}{d(0)}. \quad (27)$$

If a bounded orbit has an exponentially increasing FLI with time  $\log_{10} \tau$ , it is chaotic. When a bounded orbit has an algebraically increasing FLI, it is ordered. The different deviation of two adjacent orbits with time is used to distinguish between chaotic and regular dynamics. The FLIs in Figure 2 (b) also describe different dynamical behaviors of Orbits 1 and 2.

In what follows, we use the methods of FLIs and Poincaré map to trace the influences of the coupling constants  $c_{13}$  and  $c_{14}$  on the transition from regular to chaotic dynamics. This consideration is based on Case (ii) with  $0 \leq 2c_{13} < c_{14} < 2$  and Case (iii) with  $0 \leq c_{14} < 2c_{13} < 2$ .

In fact, the coupling constants  $c_{13}$  and  $c_{14}$  considered in Figure 1 correspond to one of the RN type black holes in Case (ii) with  $0 \leq 2c_{13} < c_{14} < 2$ . In this case, we continue our numerical simulations by taking the parameters  $b = 9.7 \times 10^{-4}$ ,  $E = 0.994$  and  $L = 4.6$  with the initial separation  $r = 35$ . Given  $c_{14} = 1.4$ , the values of  $c_{13} = 0.05, 0.25$  and  $0.40$  correspond to the existence of order, weak chaos and strong chaos in Figure 3 (a)-(c). Although the orbits seem to be seven-island orbits for  $c_{13} = 0.05$  and  $0.25$  from the Poincaré map,  $c_{13} = 0.05$  indicates the regular dynamics and  $c_{13} = 0.25$  yields the chaotic dynamics from the FLIs in Figure 3 (d). These facts seem to show that the transition from regular to chaotic dynamics occurs easily and chaos becomes stronger as the coupling constant  $c_{13}$  increases. On the other hand, an increase of the coupling constant  $c_{14}$  seems to suppress the occurrence of chaos and to weaken the extent of chaos when the coupling constant  $c_{13} = 0.3$  is given in Figure 3 (e)-(h).

Figure 4 describes the phase space structures of orbits for several values of  $c_{14}$  or  $c_{13}$  in Case (iii) with  $0 \leq c_{14} < 2c_{13} < 2$  corresponding to non-RN black holes, where  $b = 9.4 \times 10^{-4}$ ,  $E = 0.994$ ,  $L = 4.8$  and  $r = 35$ . In Figure 4 (a)-(c),  $c_{14} = 0.1$  and  $c_{14} = 0.3$  yield regular dynamics, but  $c_{14} = 0.4$  exhibits chaotic dynamics for  $c_{13} = 0.50$ . When  $c_{14} = 0.4$  is given in Figure 4 (c)-(e),  $c_{13} = 0.50, 0.54$  and  $0.65$  correspond to strong chaos, weak chaos and order in sequence. This fact can also be seen clearly from the FLIs in Figure 4 (f).

Figure 5 (a) plots the dependence of the FLI on the coupling parameter  $c_{13}$  in Case (ii), where the other parameters and the initial separation are those of Figure 3 (d). Each FLI is computed until the integration time reaches  $1 \times 10^6$ . 5 is the threshold of the FLI between chaos and order. That is, all FLIs less than 5 indicate the regularity, whereas those larger than or equal to 5 show the chaoticity. Chaos occurs almost everywhere for  $c_{13} > 0.2611$  in Figure 5 (a). On the other hand, there is chaos almost everywhere for  $c_{14} < 1.4302$  with  $c_{13} = 0.3$  in Figure 5 (b). The two cases in Figure 5 (a) and (b) are considered together in Figure 6 (a) that lists a distribution of order and chaos in the binary parameter space  $(c_{13}, c_{14})$ . The region under the line  $c_{14} = 0.7767c_{13} + 1.1972$

is chaotic almost everywhere, while the region over the line is almost regular. The dynamics in Case (iii) is unlike that in Case (ii). Chaos occurs mainly for  $c_{13} < 0.5396$  with  $c_{14} = 0.4$  in Figure 5 (c), and so does it for  $c_{14} > 0.2610$  with  $c_{13} = 0.5$  in Figure 5 (d). The two cases in Figure 5 (c) and (d) can be shown together through the distribution of order and chaos in the binary parameter space  $(c_{13}, c_{14})$  in Figure 6 (b). The main chaotic region is over the line  $c_{14} = 3.5155c_{13} - 1.4968$ , and the ordered region is mainly below the line.

Replacing  $b$ ,  $E$  and  $L$  in Figure 6 (a) with  $b = 9.1 \times 10^{-4}$ ,  $E = 0.995$  and  $L = 4.8, 5.0, 5.2$ , we give distributions of order and chaos in the binary parameter space  $(c_{13}, c_{14})$  in Figure 7 (a)-(c). Based on Case (ii), the distributions are typically different for distinct values of the angular momentum  $L$ . When Case (ii) gives place to Case (iii) in Figure 7 (d)-(f), the dependence of chaotic dynamics on  $c_{13}$  or  $c_{14}$  is varied with the variation of  $L$ . The chaotic region is enlarged as the angular momentum  $L$  increases. The result is unlike that of Refs. [44,45] on the increase of  $L$  weakening the degree of chaos.

Figure 8 (a)-(c) relates to the distributions of order and chaos for several different values of the magnetic parameter  $b$  with  $L = 4.7$  and  $E = 0.995$  in Case (ii). The chaotic region increases with the magnetic parameter  $b$  increasing. This result is also suitable for the increase of energy  $E$  in Figure 9 (a)-(c) and initial radius  $r$  in Figure 10 (a)-(c). The distributions of order and chaos for several values of  $b$ ,  $E$  or  $r$  in Case (iii) (i.e., Figures 8-10 (d)-(f)) are different from those in Case (ii).

In short, no universal rule can be given to the dependence of regular and chaotic dynamics on varying one or two parameters  $c_{13}$  and  $c_{14}$  in Cases (ii) and (iii). The distributions of order and chaos in the binary parameter space  $(c_{13}, c_{14})$  are different when different combinations of the other parameters  $E$ ,  $L$ ,  $b$  and the initial radius  $r$  are considered. This result should be reasonable because not only one or two parameters but also a combination of the other parameters and the initial conditions are responsible for the occurrence of chaos.

#### 4. Conclusion

The Einstein-Æther gravity is a covariant theory of gravity violating the local Lorentz symmetry. In the Einstein-Æther metric describing a non-rotating black hole, there are two free parameters  $c_{13}$  and  $c_{14}$ . This metric corresponds to the RN black hole solution when the two free parameters satisfy the condition  $0 \leq 2c_{13} < c_{14} < 2$ , but it is a non-RN black hole solution for the case of  $0 \leq c_{14} < 2c_{13} < 2$ . The spacetime is integrable in the two cases. When the black hole is immersed in an external asymptotically uniform magnetic field, the dynamic of charged particles moving around the non-rotating black hole is not integrable.

There are five explicitly integrable splitting terms in the Hamiltonian system describing the motion of charged test particles around the Einstein-Æther black hole surrounded by the external magnetic field. This gives a good chance for the construction of explicit symplectic integrators. Numerical tests show that the established second- and fourth-order explicit symplectic methods exhibit excellent long-term performance in accuracy of conserving the Hamiltonian. The fourth-order explicit symplectic scheme is chosen to investigate the dynamics of charged particles.

There is no universal rule for the dependence of regular and chaotic dynamics on varying one or two parameters  $c_{13}$  and  $c_{14}$  in the two cases of  $0 \leq 2c_{13} < c_{14} < 2$  and  $0 \leq c_{14} < 2c_{13} < 2$ . The distributions of order and chaos in the binary parameter space  $(c_{13}, c_{14})$  rely on different combination of the other parameters and the initial conditions.

**Author Contributions:** C.L. made contributions to the software, writing — original draft, and methodology. X.W. contributed to the supervision, conceptualization, writing — review and editing, and funding acquisition. All authors have thoroughly reviewed and approved the published version of the manuscript.

**Funding:** This research has been supported by the National Natural Science Foundation of China (Grant No. 11973020) and the National Natural Science Foundation of Guangxi (No. 2019GXNSFDA245019).

**Data Availability Statement:** The study does not report any data.

**Conflicts of Interest:** The authors declare no conflict of interest.

## REFERENCES

- [1] Abbott, B.P.; Abbott, R.; Abbott, T.D., et al. Observation of Gravitational Waves from a Binary Black Hole Merger. *Phys. Rev. Lett.* **2016**, *116*, 061102.
- [2] Akiyama, K.; Alberdi, A.; Alef, W., et al. First M87 Event Horizon Telescope Results. I. The Shadow of the Supermassive Black Hole. *The Astrophysical Journal Letters* **2019**, *875*, L1.
- [3] Wagoner, R.V. Scalar tensor theory and gravitational waves, *Physical Review D* **1970**, *1*, 3209-3216.
- [4] Deng, X.-M.; Xie, Y. Solar System tests of a scalar-tensor gravity with a general potential: Insensitivity of light deflection and Cassini tracking. *Physical Review D* **2016**, *93*(4), 044013
- [5] Moffat, J.W. Scalar tensor vector gravity theory. *J. Cosmol. Astropart. Phys.* **2006**, *3*, 4. arXiv: gr-qc/0506021.

- [6] Skordis, C. The tensor-vector-scalar theory and its cosmology. *Classical and Quantum Gravity* **2009**, 26, 143001
- [7] Horava, P. Spectral Dimension of the Universe in Quantum Gravity at a Lifshitz Point. *Phys. Rev. Lett.* **2009**, 102.161301
- [8] Deng, X.-M.; Xie, Y. Improved upper bounds on Kaluza-Klein gravity with current Solar System experiments and observations. *European Physical Journal C* **2015**, 75,539.
- [9] Katore, S. D.; Hatkar, S. P.; Tadas, D. P. Accelerating Kaluza-Klein Universe in Modified Theory of Gravitation. *Astrophysics* **2023**, 66, 98.
- [10] Sotiriou, T. P.; Faraoni, V. f(R) theories of gravity. *Reviews of Modern Physics* **2010**, 82, 451.
- [11] Gao, B.; Deng, X.-M. Dynamics of charged test particles around quantum-corrected Schwarzschild black holes. *European Physical Journal C* **2021**, 81, 983.
- [12] Jacobson, T.; Mattingly, D. Einstein-æther gravity: a status report. *Physical Review D* **2001**, 64, 024028.
- [13] Ding, C.; Wang, A.; Wang, X. Charged Einstein-Æther black holes and Smarr formula. *Physical Review D* **2015**, 92, 084055.
- [14] Rayimbaev, J.; Abdujabbarov, A.; Jamil, M., et al. Dynamics of magnetized particles around Einstein-Æther black hole with uniform magnetic field. *Nuclear Physics B* **2021**, 966, 115364.
- [15] Clifton, T.; Ferreira, P.G.; Padilla, A.; Skordis, C. Modified gravity and cosmology. *Physics Reports* **2012**, 513, 1-189.
- [16] Nojiri, S.; Odintsov, S. D. Unified cosmic history in modified gravity: From F(R) theory to Lorentz non-invariant models. *Physics Reports* **2011**, 505, 59.
- [17] Nojiri, S.; Odintsov, S. D.; Oikonomou, V.K. Modified gravity theories on a nutshell: Inflation, bounce and late-time evolution. *Physics Reports* **2017**, 692, 1-104.
- [18] Esteban, E.P.; Medina, I.R. Accretion onto black holes in external magnetic fields. *Physical Review D* **1990**, 42, 307.
- [19] de Felice, F.; Sorge, F. Magnetized orbits around a Schwarzschild black hole. *Classical and Quantum Gravity* **2003**, 20, 469–481.

- [20] Abdujabbarov, A.; Ahmedov, B.; Rahimov, O.; Salikhbaev, U. Magnetized particle motion and acceleration around a Schwarzschild black hole in a magnetic field. *Phys. Scr.* **2014**, *89*, 084008.
- [21] Kološ, M.; Stuchlík, Z.; Tursunov, A. Quasi-harmonic oscillatory motion of charged particles around a Schwarzschild black hole immersed in a uniform magnetic field. *Classical and Quantum Gravity* **2015**, *32*, 165009.
- [22] Shaymatov, S.; Patil, M.; Ahmedov, B.; Joshi, P.S. Destroying a near-extremal Kerr black hole with a charged particle: Can a test magnetic field serve as a cosmic censor? *Physical Review D* **2015**, *91*, 064025.
- [23] Tursunov, A.; Stuchlík, Z.; Kološ, M. Circular orbits and related quasiharmonic oscillatory motion of charged particles around weakly magnetized rotating black holes. *Physical Review D* **2016**, *93*, 084012.
- [24] Lin, H.-Y.; Deng, X.-M. Rational orbits around 4 D Einstein-Lovelock black holes. *Physics of the Dark Universe* **2021**, *31*, 100745.
- [25] Gao, B.; Deng, X.-M. Bound orbits around modified Hayward black holes. *Modern Physics Letters A* **2021**, *36*, 2150237.
- [26] Deng, X.-M. Geodesics and periodic orbits around quantum-corrected black holes. *Physics of the Dark Universe* **2020**, *30*, 100629.
- [27] Deng, X.-M. Periodic orbits around brane-world black holes. *European Physical Journal C* **2020**, *80*, 489.
- [28] Gao, B.; Deng, X.-M. Bound orbits around Bardeen black holes. *Annals of Physics* **2020**, *418*, 168194.
- [29] Odintsov, S. D.; Oikonomou, V. K. Dissimilar donuts in the sky? Effects of a pressure singularity on the circular photon orbits and shadow of a cosmological black hole. *Europhysics Letters* **2022**, *139*, 59003.
- [30] Chakraborty, S. Bound on Photon Circular Orbits in General Relativity and Beyond. *Galaxies* **2021**, *9*, 96.
- [31] Qiao, C.-K.; Li, M. Geometric approach to circular photon orbits and black hole shadows. *Physical Review D* **2022**, *106*, L021501.
- [32] Nakamura, Y.; Ishizuka, T. Motion of a Charged Particle Around a Black Hole Permeated by Magnetic Field and its Chaotic Characters. *Astrophys. Space Sci.* **1993**, *210*, 105–108.



- [33] Takahashi, M.; Koyama, H. Chaotic Motion of Charged Particles in an Electromagnetic Field Surrounding a Rotating Black Hole. *The Astrophysical Journal* **2009**, 693, 472.
- [34] Kopáček, O.; Karas, V.; Kovář, J.; Stuchlík, Z. Transition from Regular to Chaotic Circulation in Magnetized Coronae near Compact Objects. *The Astrophysical Journal* **2010**, 722, 1240.
- [35] Kopáček, O.; Karas, V. Inducing Chaos by Breaking Axial Symmetry in a Black Hole Magnetosphere. *The Astrophysical Journal* **2014**, 787, 117.
- [36] Stuchlík, Z.; Kološ, M. Acceleration of the charged particles due to chaotic scattering in the combined black hole gravitational field and asymptotically uniform magnetic field. *European Physical Journal C* **2016**, 76, 32.
- [37] Kopáček, O.; Karas, V. Near-horizon Structure of Escape Zones of Electrically Charged Particles around Weakly Magnetized Rotating Black Hole. *The Astrophysical Journal* **2018**, 853, 53.
- [38] Pánis, R.; Kološ, M.; Stuchlík, Z. Determination of chaotic behaviour in time series generated by charged particle motion around magnetized Schwarzschild black holes. *European Physical Journal C* **2019**, 79, 479.
- [39] Stuchlík, Z.; Kološ, M.; Kovář, J.; Tursunov, A. Influence of Cosmic Repulsion and Magnetic Fields on Accretion Disks Rotating around Kerr Black Holes. *Universe* **2020**, 6, 26.
- [40] Stuchlík, Z.; Kološ, M. Acceleration of the charged particles due to chaotic scattering in the combined black hole gravitational field and asymptotically uniform magnetic field. *European Physical Journal C* **2016**, 76, 32.
- [41] Shipley, J.O.; Dolan, S.R. Binary black hole shadows, chaotic scattering and the Cantor set. *Classical and Quantum Gravity* **2016**, 33 (17), 175001
- [42] Wang, M.; Chen, S.; Wang, J.; Jing, J. Shadow of a Schwarzschild black hole surrounded by a Bach-Weyl ring. *European Physical Journal C* **2020**, 80, 110
- [43] Wang, Y.; Sun, W.; Liu, F., et al. Construction of Explicit Symplectic Integrators in General Relativity. I. Schwarzschild Black Holes. *The Astrophysical Journal* **2021**, 907, 66.
- [44] Wang, Y.; Sun, W.; Liu, F., et al. Construction of Explicit Symplectic Integrators in General Relativity. II. Reissner-Nordström Black Holes. *The Astrophysical Journal* **2021**, 909, 22.
- [45] Wang, Y.; Sun, W.; Liu, F., et al. Construction of Explicit Symplectic Integrators in General Relativity. III. Reissner-Nordström-(anti)-de Sitter Black Holes. *Astrophys. J. Suppl. Ser.* **2021**, 254, 8.

- [46] Wu, X.; Wang, Y.; Sun, W., et al. Construction of Explicit Symplectic Integrators in General Relativity. IV. Kerr Black Holes. *The Astrophysical Journal* **2021**, 914, 63.
- [47] Wu, X.; Wang, Y.; Sun, W., et al. Explicit Symplectic Methods in Black Hole Spacetimes. *The Astrophysical Journal* **2022**, 940, 166.
- [48] Yoshida, H. Recent Progress in the Theory and Application of Symplectic Integrators. *Celestial Mechanics and Dynamical Astronomy* **1993**, 56, 27.
- [49] Froeschlé, C.; Lega, E., On the Structure of Symplectic Mappings. The Fast Lyapunov Indicator: a Very Sensitive Tool. *Celestial Mechanics and Dynamical Astronomy* **2000**, 78, 167.
- [50] Yoshida, H. Construction of higher order symplectic integrators. *Physics Letters A* **1990**, 150, 262.
- [51] Wu, X.; Huang, T.-Y. Computation of Lyapunov exponents in general relativity. *Physics Letters A* **2003**, 313, 77.
- [52] Wu, X.; Huang, T.-Y.; Zhang, H. Lyapunov indices with two nearby trajectories in a curved spacetime. *Physical Review D* **2006**, 74, 083001.

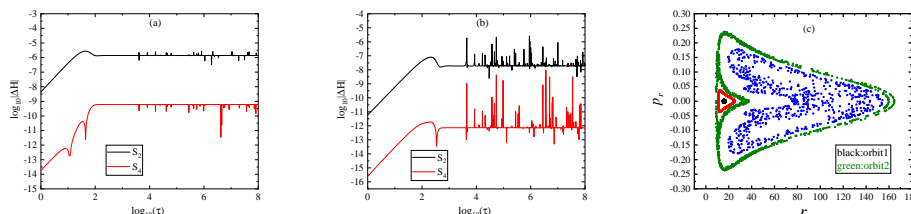


Fig. 1.— (a) Hamiltonian errors  $\Delta H = H + 1/2$  in Equation (17) for the two symplectic methods  $S_1$  and  $S_4$  acting on Orbit 1. (b) Same as (a) but Orbit 1 replaced with Orbit 2. (c) Poincaré map at the plane  $\theta = \pi/2$  with  $p_\theta > 0$ . The parameters are  $E = 0.995$ ,  $L = 4.7$ ,  $b = 9.1 \times 10^{-4}$ ,  $q = 1$ ,  $c_{13} = 0.01$  and  $c_{14} = 0.03$  in Case (ii); the initial conditions are  $p_r = 0$  and  $\theta = \pi/2$ . Orbit 1 with the initial separation  $r = 15$  is regular, whereas Orbit 2 with the initial separation  $r = 35$  is chaotic.

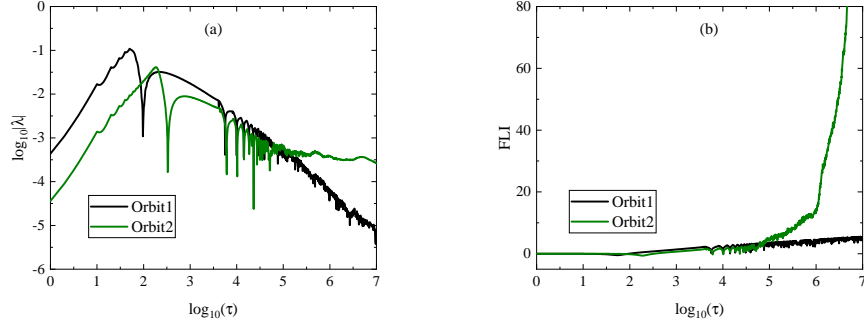


Fig. 2.— (a) The largest Lyapunov exponents  $\lambda$  for Orbits 1 and 2. (b) The fast Lyapunov indicators (FLIs) for Orbits 1 and 2.

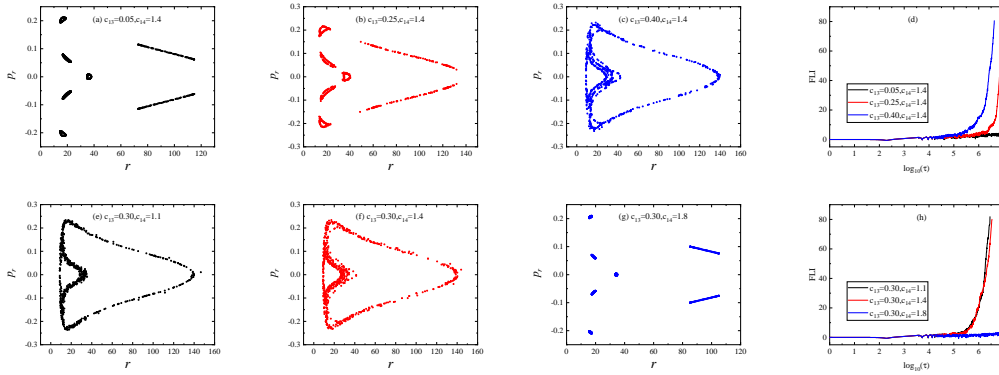


Fig. 3.— (a)-(c): Poincaré sections in Case (ii) of  $0 \leq 2c_{13} < c_{14} < 2$ . The parameters are  $b = 9.7 \times 10^{-4}$ ,  $E = 0.994$ ,  $L = 4.6$ ,  $c_{14} = 1.4$ , and  $c_{13}$  is given different values in (a)-(c). The initial radius is  $r = 35$ . (d): The FLIs for the orbits in (a)-(c). (e)-(h): Same as (a)-(d), but  $c_{13} = 0.30$  is given and  $c_{14}$  has distinct values.

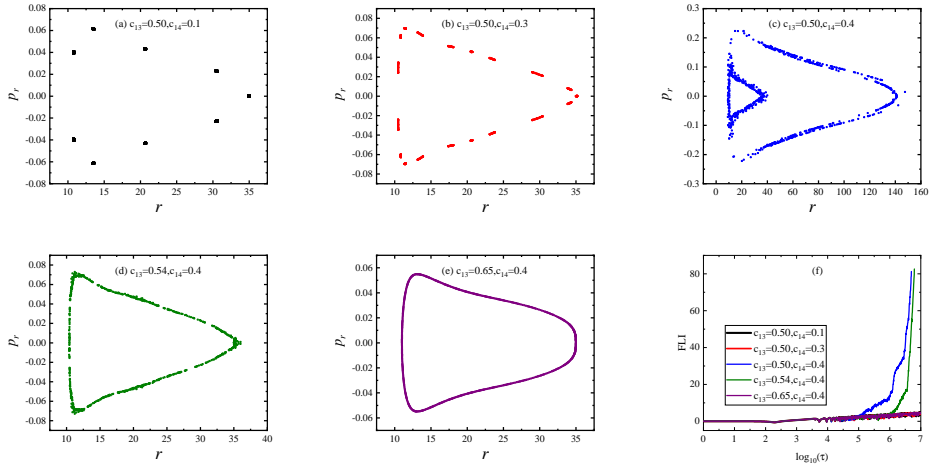


Fig. 4.— (a)-(e): Poincaré sections in Case (iii) of  $0 \leq c_{14} < 2c_{13} < 2$ . The parameters are  $b = 9.4 \times 10^{-4}$ ,  $E = 0.994$ ,  $L = 4.8$ ; the initial radius is  $r = 35$ . In (a)-(c),  $c_{13} = 0.50$ , and  $c_{14}$  has different values. In (d) and (e),  $c_{14} = 0.40$ , and  $c_{13}$  has two different values. (f): The FLIs for the orbits in (a)-(e).

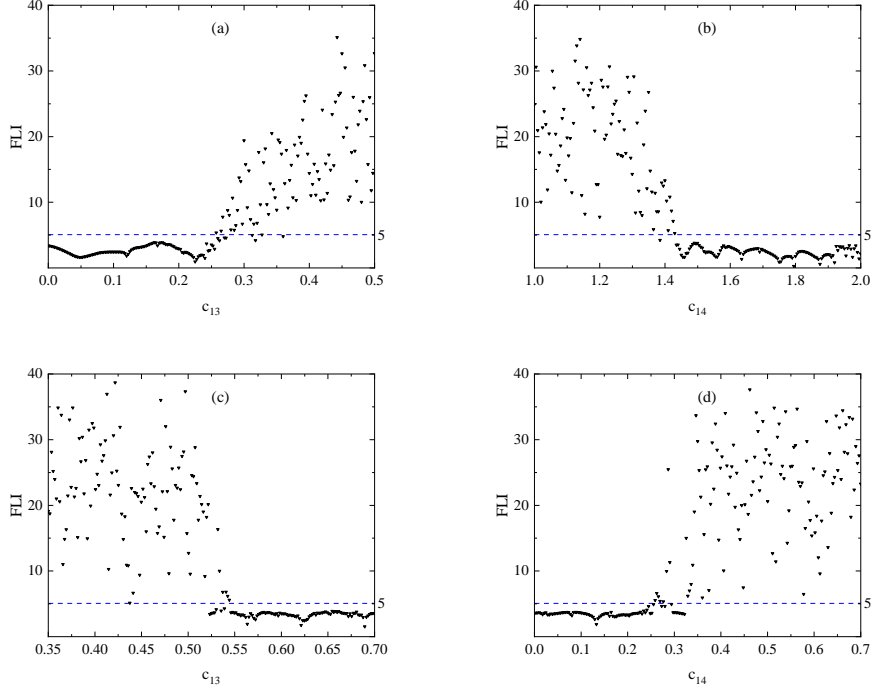


Fig. 5.— Dependence of FLI on  $c_{13}$  or  $c_{14}$ . (a) and (b): Corresponding to Figure 3.  $c_{14} = 1.4$  is fixed in (a), and  $c_{13} = 0.3$  is fixed in (b). (c) and (d): Corresponding to Figure 4.  $c_{14} = 0.4$  is fixed in (c), and  $c_{13} = 0.5$  is fixed in (d).

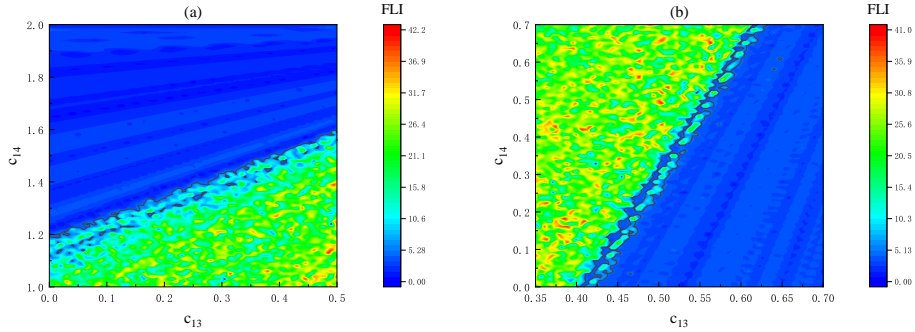


Fig. 6.— Distributions of order and chaos in the two parameter space  $(c_{13}, c_{14})$  using the FLIs. The initial radius is  $r = 35$ . (a)  $b = 9.7 \times 10^{-4}$ ,  $E = 0.994$  and  $L = 4.6$  in Case (ii). (b)  $B = 9.4 \times 10^{-4}$ ,  $E = 0.994$  and  $L = 4.8$  in Case (iii).

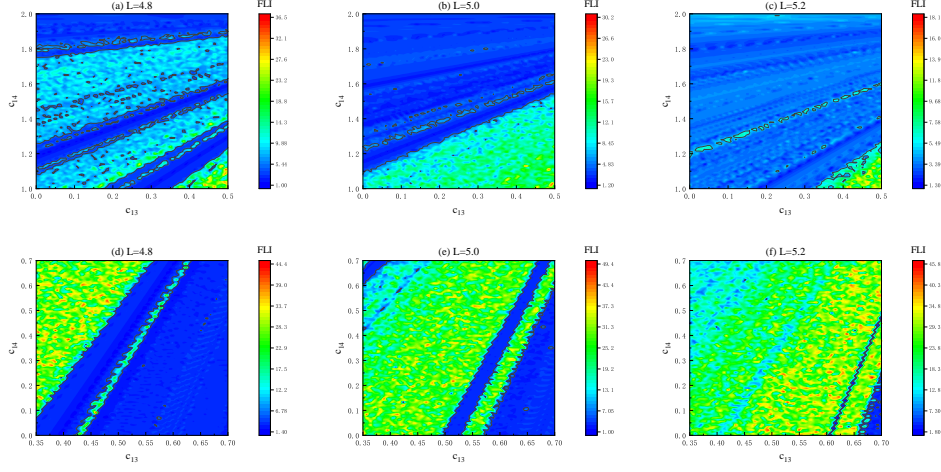


Fig. 7.— Same as Figure 6, but several values are given to the angular momentum  $L$ . The initial radius is  $r = 35$ , and the other parameters are  $b = 9.1 \times 10^{-4}$  and  $E = 0.995$ . (a)-(c): Case (ii) is considered. (d)-(f): Case (iii) is considered.

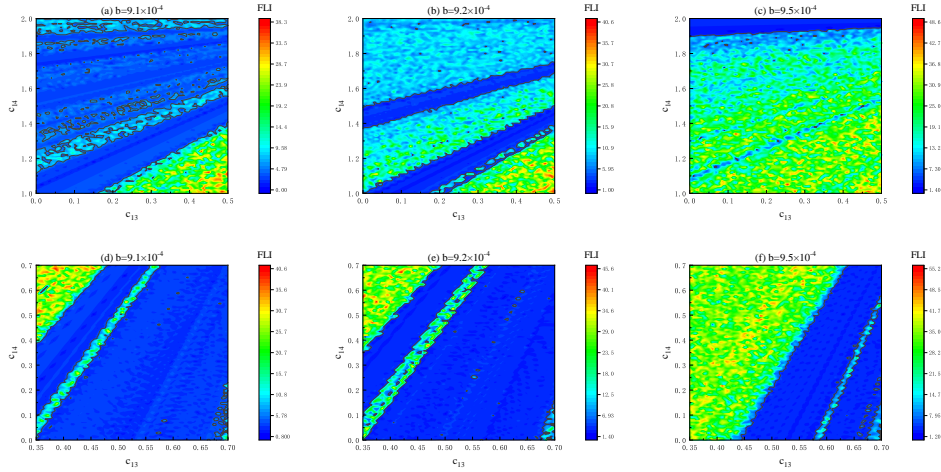


Fig. 8.— Same as Figure 7, but several values are given to the magnetic field parameter  $b$ . The initial radius is  $r = 35$ , and the other parameters are  $L = 4.7$  and  $E = 0.995$ . (a)-(c): Case (ii). (d)-(f): Case (iii).

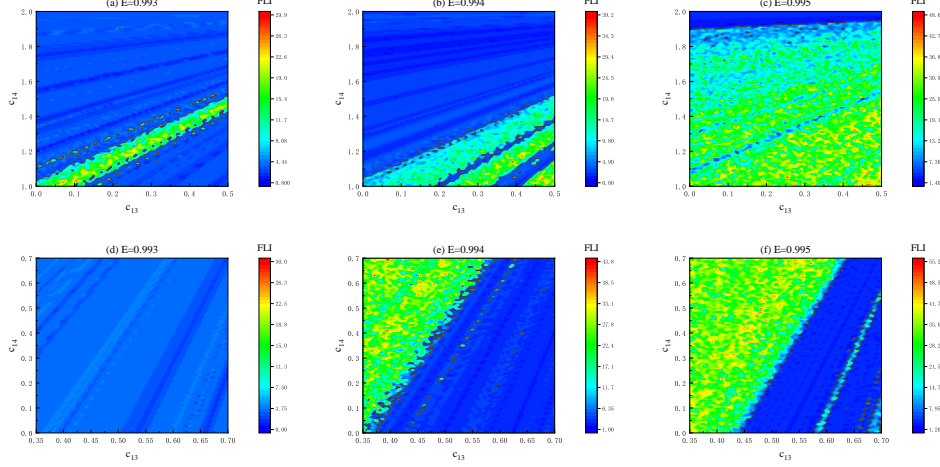


Fig. 9.— Same as Figure 8, but several values are given to the energy  $E$ . The initial radius is  $r = 35$ , and the other parameters are  $b = 9.5 \times 10^{-4}$  and  $L = 4.7$ . (a)-(c): Case (ii). (d)-(f): Case (iii).

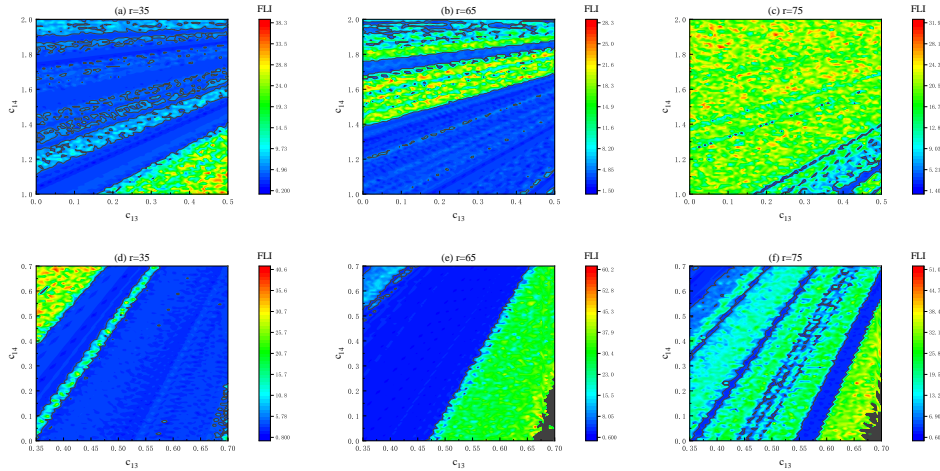


Fig. 10.— Same as Figure 9, but several values are given to the initial radius  $r$ . The other parameters are  $b = 9.1 \times 10^{-4}$ ,  $E = 0.995$  and  $L = 4.7$ . (a)-(c): Case (ii). (d)-(f): Case (iii).